

A Non-Stationary Channel Model for the Development of Non-Wearable Radio Fall Detection Systems

Alireza Borhani, *Member, IEEE* and Matthias Pätzold, *Senior Member, IEEE*

Abstract—The emerging non-wearable fall detection systems rely on processing radio waves reflected off the body of the home user who has no active interaction with the system, increasing the user privacy and acceptability. This paper proposes a non-stationary channel model that is important for the development of such systems. A three-dimensional stochastic trajectory model is designed to capture targeted mobility patterns of the home user. The model is featured with a forward fall mechanism, which is actuated at a random point along the path. A transmitter emits radio waves throughout an indoor propagation environment, while a receiver collects fingerprints of the scattering objects on the emitted waves. The corresponding radio channel is modelled by a process capturing the time-variant Doppler effect caused by the home occupant. The time-frequency behaviour of the non-stationary channel is studied by computing the Doppler power spectral density and by performing spectrogram analysis. The instantaneous mean Doppler shift and Doppler spread are derived and simulated. The model is confirmed with experimental results performed at 5.9 GHz. The results are insightful for developing reliable fall detection algorithms, while the model is useful for studying the impact of different walking/falling patterns on the overall fall detection system performance.

Index Terms — Non-stationary radio channels, random trajectory model, power spectral density, spectrogram, instantaneous mean Doppler shift

I. INTRODUCTION

The world population is growing older and older, as fertility rates are low in most world regions. From 2025 to 2050, the 65+ year old population is projected to almost double to 1.6 billion globally, while the total population will grow by just 34 percent over the same period [1]. According to the World Health Organization [2], around one-third of people aged 65+ years fall at least twice a year. One of the main challenges within eldercare is thus detecting fall incidents for those who live independently. Such incidents may result in serious physical and psychological consequences, if not in Kodokushi¹ cases. To avoid such consequences, there is a need to design elderly-friendly activity monitoring technologies and services that can reliably and immediately detect in-home incidents, allowing for timely emergency actions that save both health and wealth.

Manuscript received January 4, 2018; revised May 16, 2018 and September 4, 2018; accepted September 5, 2018. The associate editor coordinating the review of this paper and approving it for publication was Prof. T. Pratt.

A. Borhani and M. Pätzold are with the Faculty of Engineering and Science, University of Agder, 4898 Grimstad, Norway (e-mails: {alireza.borhani, matthias.patzold}@uia.no).

¹Kodokushi or lonely death refers to a Japanese phenomenon of people dying alone and remaining undiscovered for a long period.

Existing fall detection systems are categorized into two major classes [3]: wearable systems and context-aware systems. Wearable systems such as smartphones, waist belts, bracelets, pendants (e.g., Lifeline by Philips² and Angel4 by SENSE4CARE³) are equipped with diverse sensors, but mostly accelerometers. Context-aware systems are non-wearable devices and facilities, such as vision sensors [4], video cameras [5], and smart floors [6]. Informative surveys on fall detection systems and approaches can be found, e.g., in [7]–[9]. The wearable systems bring about several user-end concerns, such as privacy, acceptability, and user training needs, yet the most important one is the need for direct involvement of the user in the solution. This solution simply fails if the user forgets/ignores to wear the device. The context-aware systems are often expensive, while their functionality is restricted to those areas in which sensors have been previously deployed. Video surveillance systems compromise the user privacy, while vision sensors have short proximity ranges [10].

Motivated by the aforementioned restrictions, a new generation of context-aware fall detection systems is emerging. In the new approach, a transmitter emits radio waves in the home environment, while a receiver collects the waves carrying fingerprints of user activities at home. Indeed, the radio waves are modulated by the scattering effects of not only fixed objects in the environment, but also the mobile home user. The challenge of the new approach is to perform sophisticated signal processing techniques to extract those fingerprints and to distinguish irregular activities, such as a fall, from other daily life activities of the user. In this context, a fall detection system based on the principles of Doppler radars was proposed in [11] and [12]. The authors of [3] exploited combined range-Doppler features to propose a more reliable fall detection system. The use of a multiple range-Doppler radar for increasing the reliability of the fall detection system was proposed very recently in [13]. In order to monitor the daily behaviour of individuals at risk of deteriorating physical or cognitive health, analysis of radar signatures for fall detection and classification of human indoor activities has been presented in [14]. The system proposed in [15] applies the frequency distribution trajectories corresponding to the velocities of the movements while falling to a hidden Markov model. In [16], the signal strength data collected from an RFID sensor was used for activity recognition purposes. In [17], an ultra-wide

²see <https://www.lifeline.philips.com/safety-solutions.html>

³see <http://www.sense4care.com/en/products/angel4-whiteblack>

band (UWB) radar was used to detect the fall incident based on the temporal characteristics of the channel. The authors of [18] studied the radio characteristics of a measured channel at 5.9 GHz to detect in-home fall incidents. A theoretical study on the influence of walking people on the Doppler spectral characteristics of indoor channels can also be found in [19]. The WiFall system [20] analyzes the channel state information (CSI) of an off-the-shelf WiFi access point to detect irregular activities at home. In this approach, the CSI tool released by Halperin et al. is very beneficial, allowing for detailed measurements of the wireless channel along with received 802.11 packet traces [21]. Different from the received signal strength indicator (RSSI), capturing merely the total received power, the CSI contains detailed information about of each subcarrier and the corresponding power delay profile [22]–[25]. A comprehensive survey of activity recognition systems based on the aforementioned approaches can be found in [26]. The radio tomographic imaging approach has also been used for fall detection purposes. In this approach a radio sensor network is employed to measure the link attenuation caused by moving objects, followed by applying a hidden Markov model to detect irregular variations caused by the fall incident [27]. A hidden Markov model-based detection approach has also been applied to RSSI collected from a dense network of WiFi compliant radio devices (operating at 2.4GHz) installed in a shared workspace [28]. More recently, Kianoush et al. has proposed a real-time system that leverages RSSI for human body motion sensing with focus on joint body localization and fall detection [29].

The new fall detection approach is still in its early stages of development and requires fundamental research studies to become mature enough before entering the production phase. One of the key existing gaps in the literature is a sound analytical channel model and the corresponding simulation model that can accurately capture the non-stationarity of the underlying real-world radio channel. The majority of the existing literature build directly on empirical data collected from very site-specific and scenario-dependent measurement campaigns. Nonetheless, theoretical and simulation models allow us to study the underlying radio channel under a variety of propagation conditions, operating frequencies, transmitter/receiver locations, and user mobility patterns just to name a few. In addition, they enable us to study and compare different metrics (channel characteristics) for developing reliable fall detection algorithms. They also give us the opportunity to conduct more insightful measurement campaigns and field trials.

To fill the aforementioned gap, this paper develops a non-stationary indoor radio channel model that allows for investigating fingerprints of the home user on the channel characteristics and for studying the responsiveness of those characteristics to multi-scale variations of the channel. We design a stochastic trajectory model to capture both targeted and non-targeted mobility patterns of the user in the three-dimensional (3D) space. The model is featured with an optional forward fall mechanism that can simulate a fall at a random point along a walking path if actuated. A fixed-to-fixed (F2F) communications scenario in the presence of some fixed scatterers due

to static objects in the environment and a cluster of moving scatterers, accounting for the body of home user, is considered. A stochastic process is proposed for modelling the time-variant (TV) multipath fading effect caused by both fixed objects and the cluster of moving objects at home. Analytical expressions for the spectral properties of the channel are derived and their responsiveness to variations of the channel is studied. It is shown that the Doppler power spectral density (PSD) is clearly fingerprinted by the fall incident. The results are verified by performing spectrogram analysis as an alternative approach to study the time-frequency behaviour of the non-stationary channel. Moreover, it is demonstrated that the instantaneous mean Doppler shift and the instantaneous Doppler spread contain very useful information about the mobility pattern of the home user. A non-falling scenario in which the user walks safely through the propagation area is also examined, showing that the spectral properties of the channel change in a much smaller order, but is still traceable. The model is verified by the experimental results collected from a measurement campaign conducted at 5.9 GHz [18].

The novelty of this paper arises not only from the proposed non-stationary channel model itself, but also from the embedded 3D stochastic trajectory model. This model is an extension of the highly flexible 2D trajectory model based on the first primitive of Brownian fields (BFs) [30], to which a third dimension is added to account for sinusoidal oscillations of a walking person along the vertical axis. The model captures key kinematical features of a walking person [31], and gives a fully time-independent trajectory, to which different speed scenarios can be applied. In this paper, we focus on a single realization of the proposed stochastic trajectory model. Nonetheless, the model proposed in this paper gives the opportunity of analyzing the statistical properties of the channel under a large number of trajectories. It is emphasized that this paper does not aim at designing fall detection algorithms, but introducing theoretically sound channel characteristics that can be used for fall detection algorithm design purposes.

The remainder of this paper is organized as follows. Section II introduces the 3D stochastic trajectory model, while Section III employs that model to develop an in-home radio propagation channel model. The complex channel gain of the proposed non-stationary channel model is presented in Section IV, while its spectral properties are investigated in Section V. Section VI demonstrates the simulation results and verifies the model. Eventually, Section VIII concludes the paper and outlines future research lines.

II. HUMAN WALKING TRAJECTORY MODEL

A. Modelling a Random Walk Without a Fall

In [30], a 2D trajectory model based on the primitives of BFs was developed to capture the trajectory \mathcal{T}_{2D} of a mobile station starting from (x_s, y_s) and terminating at or in the vicinity of a predefined destination point (x_d, y_d) . The random trajectory \mathcal{T}_{2D} based on the first primitive of BFs is given by the following set of pairs

$$\mathcal{T}_{2D} := \left\{ (\mathbf{x}(l), \mathbf{y}(l)) \mid \begin{array}{l} \mathbf{x}(l) = x_s + k_d l \delta_x + \sigma_x \mathbf{W}_x(l, k_b) \\ \mathbf{y}(l) = y_s + k_d l \delta_y + \sigma_y \mathbf{W}_y(l, k_b) \end{array} \right\} \quad (1)$$

where $l = 1, 2, \dots, L$ denotes the position index, and L represents that of the terminating point. The terms $\delta_x = (x_d - x_s)/L$ and $\delta_y = (y_d - y_s)/L$ stand for the deterministic increments along the x - and y -axis, respectively. The parameter k_d is a drift switch to control the presence of a predefined drift evolving the trajectory towards the destination point (x_d, y_d) . The parameter σ_x (σ_y) controls the randomness of the trajectory process ${}_p\mathbf{x}(l)$ (${}_p\mathbf{y}(l)$) along the x -axis (y -axis).⁴ Furthermore, the partial random bridge $\mathbf{W}_x(l, k_b) = {}_1\mathbf{B}_x(l) - \frac{k_b l}{L} {}_1\mathbf{B}_x(L)$ models the randomness of the trajectory along each axis by means of the first primitive ${}_1\mathbf{B}_x(l)$ of the standard BF $\mathbf{B}_x(l)$ associated with the x -axis. The bridge parameter k_b accounts for the integration degree of the bridge to the destination point.

It is known from the kinematics of walking (gait cycle) [31] that the apparent height $z(l)$ of a walking person can be best modelled by the sinusoidal function

$$z(l) = z_h + \alpha_h \cos(\omega_G l + \theta_0) \quad (2)$$

where z_h is the actual height of the underlying body part, α_h is an experimental parameter proportional to the actual height H of the person, θ_0 is a uniformly distributed initial phase, and ω_G determines the frequency of oscillations along the z -axis. Herein, it is assumed that the trajectory of a sample scatterer (a body part) along the z -axis is also modelled by a similar sinusoidal function that has been lifted to the corresponding height (of that body part).

We extend that the two-dimensional (2D) model in (1) by adding a third dimension according to (2) to account for vertical oscillations of the walking person along the z -axis. The resulting extended 3D human walking trajectory \mathcal{T}_{3D} can then be determined by the following set of triples⁵

$$\mathcal{T} := \left\{ (\mathbf{x}(l), \mathbf{y}(l), z(l)) \left| \begin{array}{l} \mathbf{x}(l) = x_s + k_d l \delta_x + \sigma_x \mathbf{W}_x(l, k_b) \\ \mathbf{y}(l) = y_s + k_d l \delta_y + \sigma_y \mathbf{W}_y(l, k_b) \\ z(l) = z_h + \alpha_h \cos(\omega_G l + \theta_0) \end{array} \right. \right\}. \quad (3)$$

The extended trajectory \mathcal{T} in (3) allows for different horizontal configurations of the path arriving at: 1) a predefined destination point (x_d, y_d) in the horizontal plane if $k_b = k_d = 1$; 2) a predefined target zone with a known radius and centre if $0 < k_b < 1$; 3) a totally random point if $k_b = 0$; or 4) the starting point (x_s, y_s) when modelling a circularly closed loop path using $k_b = 1$ and $k_d = 0$. Therefore, the model in (3) is very useful for analyzing the impact of different mobility patterns of the home user on the underlying radio channel model.

In this paper, we focus on a special case of the random trajectory in (3), in which $k_b = k_d = 1$ and $\sigma_x = \sigma_y$, meaning that the trajectory is fully targeted towards a predefined destination point, while the variations (controlled by $\sigma_{(\cdot)}$) of the trajectory in the horizontal plane are statistically symmetric. In this case, the maximum distance σ_{\max} from the shortest trajectory (straight path) equals $\sigma_x \sqrt{L^3/48}$ [32]. This special case results in very focused TV angle-of-motions (AOMs) (see

⁴Note that due to the symmetry of the proposed trajectory model in the horizontal plan, the statistical characteristics of $\mathbf{x}(l)$ and $\mathbf{y}(l)$ are the same.

⁵For the sake of brevity, henceforth we use \mathcal{T} in place of \mathcal{T}_{3D} .

Fig. 7 in [32]) towards the predefined destination point. This property of the trajectory will help us to design a forward fall mechanism.

A single realization of (3) generates a master trajectory \mathcal{T} . It is assumed that this master trajectory explains the spatial behavior of each body part if it is shifted to the corresponding starting point (x_s, y_s, z_h) (associated with that body part). Herein, the number of N_M moving scatterers (starting points) is considered. The corresponding trajectories are then denoted by $\mathcal{T}_1, \mathcal{T}_2, \dots, \mathcal{T}_{N_M}$.

B. Modelling a Random Walk with Forward Fall

To this aim, we consider a rounded outcome of the uniform distribution between 1 and L as the position index l_{FP} of the fall point. It is assumed that the falling phase happens within $l_{FP} \leq l \leq l_{FP} + L_F$, where L_F is the length of the falling phase. This can be supported by the measurement studies in [33], showing that both the vertical speed S_v and the horizontal speed S_h of a walking person starts increasing some milliseconds before the actual fall and keeps increasing until the fall is completed.

Let $z_{n_M}(l)$ denote the time-varying height of the n_M th moving scatterer (body part). Then, running the recursive equation

$$z_{n_M}(l) = z_{n_M}(l-1) - z_{n_M}(l_{FP})/L_F \quad (4)$$

for $l_{FP} + 1 \leq l \leq l_{FP} + L_F$ reduces the height to zero within L_F steps.

Accordingly, the height reduction mechanism above is applied to N_M sample trajectories $\mathcal{T}_1, \mathcal{T}_2, \dots, \mathcal{T}_{N_M}$ associated with the N_M moving scatterers. It is assumed that the fall point index l_{FP} is the same across all these trajectories. Given the special case $k_b = k_d = 1$ discussed in Sec. II-A, the horizontal evolvment of the path (the azimuth AOM) is statistically towards a particular destination point (see Fig. 7 in [32]). Such a horizontal evolvment combined with the proposed height reduction mechanism assures the generation of a forward fall along the intended path.

It is noteworthy that at the end of a real fall, different body parts (scatterers) will not have a zero-level height. Given the fact that those scatterers become motionless at the end of the fall, such detailed consideration does not have any major impact on the time-frequency behavior of the channel. With this in mind, we assume that when the falling phase is completed, the N_M scatterers are at the floor level (zero height). This helps us to reduce the model complexity by ignoring less important factors (in this particular context).

C. Extension to Arbitrary Speed Profiles

A novel feature of \mathcal{T} in (3) is its fully spatial formulation in position, rather than time. This gives the chance of applying arbitrary speed scenarios to a particular path configuration.

Let us focus on a non-falling scenario. The 3D trajectory $\mathcal{T}_{(\cdot)}$ of the user is obtained by connecting the L points, i.e., $(x(l), y(l), z(l))$ ($l = 1, 2, \dots, L$) generated by (3). Hence, there exist $L - 1$ incremental sub-trajectories that connect pairs of consecutive points. An arbitrary speed of $s_{n_M, l}^h$

$(s_{n_M,l}^v)$ can then be considered as the horizontal (vertical) speed of the n_M th body part (moving scatterer) along the l th sub-trajectory. Accordingly, an arbitrary speed vector of $[s_{n_M,1}^h, s_{n_M,2}^h, \dots, s_{n_M,L-1}^h; s_{n_M,1}^v, s_{n_M,2}^v, \dots, s_{n_M,L-1}^v]$ can be mapped to the whole 3D trajectory \mathcal{T}_{n_M} , explaining the temporal behaviour of the n_M th moving scatterer (associated with the walking person) along the path.

For the falling scenario, the whole trajectory is divided to three phases, namely the walking phase, falling phase, and the lying-on-the-floor phase. An arbitrary matrix $[s_{n_M,1}^h, \dots, s_{n_M,l_{FP}-1}^h; s_{n_M,1}^v, \dots, s_{n_M,l_{FP}-1}^v]$ is assigned to the $l_{FP} - 1$ sub-trajectories, representing the speed characteristic of the n_M th part of the body within the walking phase (before the fall). A second matrix of speeds $[s_{n_M,l_{FP}}^h, \dots, s_{n_M,l_{FP}+L_F}^h; s_{n_M,l_{FP}}^v, \dots, s_{n_M,l_{FP}+L_F}^v]$ determines the speed of the n_M th moving scatterer within the falling phase. In Sec. VI, we employ the standard speed characteristics of a walking/falling person obtained from video signal processing in [33]. After the fall, it is assumed that both the horizontal and vertical speeds of the user equal zero, thus there will be no more evolution of the path when the incident is completed.

III. PROPAGATION SCENARIO

An in-home F2F propagation scenario in which the transmitter (Tx) is set on the floor and the receiver (Rx) is mounted on the ceiling of the room is assumed (see Fig. 2)⁶. The position of the Tx (Rx) is denoted by (x^T, y^T, z^T) ((x^R, y^R, z^R)). The line-of-sight (LOS) between the Tx and the Rx is blocked intentionally. A total number of $N_F + N_M$ scatterers is assumed to be in the propagation area. The static objects in the room, including the walls, are modelled by N_F fixed scatterers (black stars in Fig.2) located at $(x_{n_F}^S, y_{n_F}^S, z_{n_F}^S)$. It is assumed that the reverberation effect between the fixed and moving scatterers does not exist. It follows that fixed scatterers are not very important, as they do not contribute to the Doppler effect⁷. A cluster of N_M moving scatterers S_n^M accounts for the parts of the body, such as the head, hands, and the legs, of the home user. We use a single realization of the random trajectory \mathcal{T} in (3) to determine the TV positions $(x_{n_M}^S(l), y_{n_M}^S(l), z_{n_M}^S(l))$ of all moving scatterers, but with slightly different starting points.

It is assumed that a plane wave emitted from the Tx with an azimuth angle-of-departure (AOD) $\alpha_n^T(l)$ and an elevation AOD $\beta_n^T(l)$ reaches the Rx with an azimuth angle-of-arrival (AOA) $\alpha_n^R(l)$ and an elevation AOA $\beta_n^R(l)$ after a single bounce scattering with the n th scatterer $S_n^{(\cdot)}$. If the n th scatterer S_n^F is fixed, none of those angles change in time.

⁶This setting is chosen to be inline with a measurement scenario that we performed. Otherwise, the model is very general and can capture various scenarios and settings.

⁷In practice, zero-Doppler frequencies might not be entirely suppressed if a frequency offset between the Tx and Rx exists. The quality of suppression is also determined by the characteristics of the designed filter. In theory, one can subtract two consecutive power delay profiles in time such that the delay contribution of the waves arriving from fixed scatterers is removed, while that of the moving objects remains.

Furthermore, it is assumed that both the Tx and the Rx are equipped with a single omnidirectional antenna.

In the non-falling scenario, it is assumed that the person walks according to \mathcal{T} and reaches successfully the planned destination point, whereas in the falling scenario, the forward fall mechanism is triggered at a random point along the path, stopping the further evolution of the trajectory after the completion of the falling phase (see Sec. II-B).

IV. MODELLING THE COMPLEX CHANNEL GAIN

To model the complex channel gain associated with the propagation scenario above, the model in [34, pp. 45–48] is extended by considering the principles of non-stationary multiple-component signals discussed in [35, pp. 19–21]. This expansion allows the Doppler frequencies $f_n(t)$ and the propagation path gains $c_n(t)$ to vary in time t or equivalently in the position index l . Accordingly, the complex channel gain $\mu(t)$ under the NLOS propagation condition is modelled at time t by the following process

$$\begin{aligned} \mu(t) &= \mu_F + \mu_M(t) = \sum_{n_F=1}^{N_F} c_{n_F} e^{j\phi_{n_F}} \\ &+ \sum_{n_M=1}^{N_M} c_{n_M}(t) e^{j \left(2\pi \int_0^t f_{n_M}(t') dt' + \phi_{n_M} \right)} \end{aligned} \quad (5)$$

representing the sum μ_F of scattered components due to the N_F fixed scatterers and the sum $\mu_M(t)$ of TV components caused by the N_M moving scatterers.⁸ In the equation above, the propagation path gain $c_{n(\cdot)}(l)$ is given by a negative path loss exponent γ applied to the total travelling distance⁹

$$\begin{aligned} D_{n(\cdot)}(t) &= D_{n(\cdot)}^{T-S}(t) + D_{n(\cdot)}^{S-R}(t) \\ &= \left((y^T - y_{n(\cdot)}^S(t))^2 + (x^T - x_{n(\cdot)}^S(t))^2 \right. \\ &+ \left. (z^T - z_{n(\cdot)}^S(t))^2 \right)^{\frac{1}{2}} + \left((y_{n(\cdot)}^S(t) - y^R)^2 \right. \\ &+ \left. (x_{n(\cdot)}^S(t) - x^R)^2 + (z_{n(\cdot)}^S(t) - z^R)^2 \right)^{\frac{1}{2}} \end{aligned} \quad (6)$$

of the $n(\cdot)$ th plane wave, i.e., $c_{n(\cdot)}(l) = C D_{n(\cdot)}^{-\gamma}(t)$, where the constant C accounts for the Tx(Rx) antenna gain, transmission power, and the wave length (see [36], [37]). For the n_F th fixed scatterer, the distance $D_{n_F}(t)$ does not change in t , thus $c_{n_F}(t) = c_{n_F}$. The phase shift $\phi_{n(\cdot)}$ in (5) is a uniformly distributed random variable between $-\pi$ and π , accounting for the physical interaction of the emitted wave with the $n(\cdot)$ th fixed/moving scatterer (see [34, p. 47] and [38, p. 59]). It is assumed that these phase shifts are independent and identically distributed random variables.

The Doppler shift $f_{n_M}(t)$ caused by the n_M th moving scatterer¹⁰ is given by

$$f_{n_M}(t) = f_{n_M,\max}(t) \left[\cos(\Theta_{n_M}^{TS}(t)) + \cos(\Theta_{n_M}^{SR}(t)) \right] \quad (7)$$

⁸The equivalent notation t_l (subscripted by the corresponding position index) will be used if such a representation helps to the clarity of the subject.

⁹The dot (\cdot) refers to the applicability of the formula/notation to both fixed and moving scatterers.

¹⁰Moving scatterers contribute to the frequency shift with a so-called double Doppler effect; once during the reception of the signal and once during its retransmission. This effect has been studied, e.g., in [39].

in which $\Theta_{n_M}^{(\cdot)}(t)$ is the TV spatial angle between the arriving (departing) wave vector at (from) the n_M th moving scatterer and the velocity of that scatterer. Fig. 1 shows the geometry of the propagation mechanism for the n_M th moving scatterer. The TV maximum Doppler frequency $f_{n_M, \max}(t)$ equals

$$f_{n_M, \max}(t) = \frac{f_0}{c_0} \sqrt{(s_{n_M, t}^h)^2 + (s_{n_M, t}^v)^2} \quad (8)$$

where f_0 denotes the carrier frequency, c_0 is the speed of light, and $s_{n_M, t}^{(\cdot)}$ represents the horizontal/vertical speed of the n_M th moving scatterer (associated with the user body) along the corresponding sub-trajectory. It is noteworthy that the actual maximum Doppler frequency is $2f_{n_M, \max}(t)$, which occurs if $\Theta_{n_M}^{TS}(t) = \Theta_{n_M}^{SR}(t) = 0$. Nonetheless, we use the traditional appearance of the maximum Doppler frequency to stay in line with the existing literature.

According to the spherical law of cosines [40, pp. 33–40], the Doppler frequency $f_n(t)$ in (7) can be rewritten in the following form

$$\begin{aligned} f_{n_M}(t) &= f_{n_M, \max}(t) \\ &\times [\sin(\beta_{n_M}^T(t)) \sin(\beta_{n_M, v}(t)) \cos(\alpha_{n_M}^T(t) - \alpha_{n_M, v}(t)) \\ &+ \sin(\beta_{n_M}^R(t)) \sin(\beta_{n_M, v}(t)) \cos(\alpha_{n_M}^R(t) - \alpha_{n_M, v}(t)) \\ &+ \cos(\beta_{n_M}^T(t)) \cos(\beta_{n_M, v}(t)) + \cos(\beta_{n_M}^R(t)) \cos(\beta_{n_M, v}(t))] \end{aligned} \quad (9)$$

in which

$$\alpha_{n_M, v}(t) = \text{atan2}(y_{n_M}^S(t_{l+1}) - y_{n_M}^S(t_l), x_{n_M}^S(t_{l+1}) - x_{n_M}^S(t_l)) \quad (10)$$

and

$$\beta_{n_M, v}(t) = \text{atan2}(z_{n_M}^S(t_{l+1}) - z_{n_M}^S(t_l), d_{n_M}(t)) \quad (11)$$

denote the TV azimuth AOM and the elevation AOM of the n_M th moving scatterer, respectively, and $\text{atan2}(y, x)$ is the four-quadrant inverse tangent function¹¹. In the equation above, the incremental distance $d_{n_M}(t)$ between two consecutive points of the trajectory \mathcal{T}_{n_M} on the horizontal plane is computed as

$$d_{n_M}(t) = \sqrt{(x_{n_M}^S(t_{l+1}) - x_{n_M}^S(t_l))^2 + (y_{n_M}^S(t_{l+1}) - y_{n_M}^S(t_l))^2}. \quad (12)$$

The angles

$$\alpha_{n_M}^T(t) = \text{atan2}(y_{n_M}^S(t) - y^T, x_{n_M}^S(t) - x^T) \quad (13)$$

and

$$\beta_{n_M}^{ST}(t) = \text{atan2}(z_{n_M}^S(t) - z^T, d_{n_M}^{ST}(t)) \quad (14)$$

represent the TV azimuth and elevation AOD from the Tx to the n th moving scatterer S_n^M , respectively, where

$$d_{n_M}^{ST}(t) = \sqrt{(x_{n_M}^S(t) - x^T)^2 + (y_{n_M}^S(t) - y^T)^2}. \quad (15)$$

¹¹Despite the inverse tangent function $\text{atan}(y/x)$, whose results are limited to the interval $(-\pi/2, \pi/2)$, the four-quadrant inverse tangent function $\text{atan2}(y, x)$ returns the angle of vector (x, y) with the positive x -axis in the range $(-\pi, \pi)$.

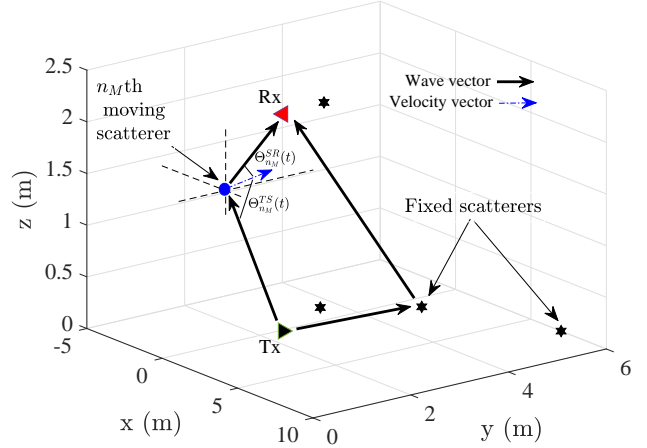


Fig. 1. The geometry of the propagation mechanism for the n_M th moving scatterer, illustrating the TV spatial angles of arrival $\Theta_{n_M}^{TS}(t)$ and departure $\Theta_{n_M}^{SR}(t)$ at and from that scatterer.

Finally, the angles $\alpha_{n_M}^R(t)$ and $\beta_{n_M}^R(t)$ stand for the TV azimuth and elevation AOA at the Rx, which can be formulated by replacing (x^T, y^T, z^T) by (x^R, y^R, z^R) in (13) and (15), respectively.

Given a sample trajectory generated by (3), all the parameters of the complex channel gain in (5) are deterministic values, except the random phases $\phi_{n_M(\cdot)}$. Nonetheless, one can step further to investigate the statistical properties of the channel by running thousands of different, yet statistically similar, trajectories generated by the same model. A guideline for studying stochastic non-stationary fading channels under the assumption of random trajectories can be found in [41].

V. SPECTRAL PROPERTIES OF THE CHANNEL

In this section, the spectral characteristics of the channel, such as the local Doppler PSD, spectrogram, instantaneous mean Doppler shift, and the instantaneous Doppler spread are studied. Further details on the behavior of these properties and their responsiveness to a fall incident will be discussed in Sec. VI.

A. Local Doppler Power Spectral Density

The local Doppler PSD explains the time-frequency behaviour of the non-stationary channel. It can be shown that the variations of the gains $c_{n_M}(t)$ are much smaller than those of the phases of $\mu_M(t)$ in (5). This assures the spectral disjointness of those two TV quantities ruling $\mu_M(t)$ (see [35, pp. 14-15]). Accordingly, the local Doppler PSD can be considered as the power-weighted distribution of Doppler shifts in time. From the deterministic TV Doppler frequency $f_{n_M}(t)$ in (9) and the path gains $c_{n_M}(t)$, the local PSD $S_f(f, t)$ of the Doppler frequencies can be approximated by

$$S_f(f, t) \approx \sum_{n_M=1}^{N_M} c_{n_M}^2(t) \delta(f - f_{n_M}(t)) \quad (16)$$

representing the impact of N_M moving scatterers on the channel spectrum. The remaining N_F fixed scatterers do not shift the carrier frequency f_0 , and thus do not contribute to the local Doppler PSD.

The drawback of this approach is the need for the direct access to detailed Doppler frequency values, which are not necessarily realizable. Nevertheless, the local PSD $S_f(f, t)$ in (16) provides a very good theoretical benchmark for other possible approaches. In what follows, a more practical method of time-frequency analysis of such a non-stationary channel is introduced.

B. Spectrogram Analysis

A second approach to study the time-frequency distribution of the channel is to perform spectrogram analysis on the complex channel gain process $\mu(t)$ in (5). This is done by first multiplying $\mu(t)$ with a sliding window function $w(t' - t)$, i.e.,

$$x(t', t) = \mu(t)w(t' - t) \quad (17)$$

where $w(t)$ is a positive even function with normalized energy, and then applying the Fourier transform to the windowed signal $x(t', t)$ with respect to t' . It follows

$$X(f, t) = \int_{-\infty}^{\infty} x(t', t)e^{-j2\pi ft'} dt' \quad (18)$$

which results in the short-time Fourier transform (STFT) of the original signal $\mu(t)$. The spectrogram $S_{xx}(f, t)$ is then defined as the squared magnitude of the STFT $X(f, t)$, i.e.,

$$S_{xx}(f, t) = |X(f, t)|^2. \quad (19)$$

In this paper, we employ the Gaussian window function $w(t)$ defined as

$$w(t) = \frac{1}{\sqrt{\sigma_\omega}\pi^{1/4}} e^{-\frac{t^2}{2\sigma_\omega^2}} \quad (20)$$

where σ_ω is called the window spread parameter. This parameter determines the time/frequency resolution of the spectral components of $S_{xx}(f, t)$. Further details on adjusting σ_ω can be found in [42].

In Sec. VI, the local Doppler PSD $S_f(f, t)$ in (16) is compared with the spectrogram $S_{xx}(f, t)$ in (19), showing that both approaches result in very similar time-frequency observations. Note that the time-frequency analysis of non-stationary multipath fading channels using the spectrogram approach is interfered with some artifacts in form of cross-terms [43]. Accordingly, the results of the two aforementioned approaches are not identical, but similar.

C. Instantaneous Mean Doppler Frequency

The instantaneous mean Doppler frequency $B_f^{(1)}(t)$ is the sum of all power-weighted Doppler shifts normalized by the total received power associated with the incoming waves. It follows [44]

$$B_f^{(1)}(t) = \frac{\sum_{n_M=1}^{N_M} c_{n_M}^2(t) f_{n_M}(t)}{\sum_{n_M=1}^{N_M} c_{n_M}^2(t) + \sum_{n_F=1}^{N_F} c_{n_F}^2(t)} \quad (21)$$

where $f_{n_M}(t)$ is given by (9).

Analogously, a second approach to compute the instantaneous mean Doppler shift is to use the spectrogram $S_{xx}(f, t)$ of the complex channel gain process $\mu(t)$. The instantaneous mean Doppler shift $B_{xx}^{(1)}(t)$ can then be formulated as [19]

$$B_{xx}^{(1)}(t) = \frac{\int_{-\infty}^{+\infty} f S_{xx}(f, t) df}{\int_{-\infty}^{+\infty} S_{xx}(f, t) df} \quad (22)$$

where $S_{xx}(f, t)$ is given by (19).

In Sec. VI, it is shown that $B_f^{(1)}(t)$ and $B_{xx}^{(1)}(t)$ closely follow each other and that of the empirical results.

D. Instantaneous Doppler Spread

The instantaneous Doppler spread $B_f^{(2)}(t)$ of the non-stationary channel can be computed by the following expression [44]

$$B_f^{(2)}(t) = \sqrt{\frac{\sum_{n_M=1}^{N_M} c_{n_M}^2(t) f_{n_M}^2(t)}{\sum_{n_M=1}^{N_M} c_{n_M}^2(t) + \sum_{n_F=1}^{N_F} c_{n_F}^2(t)} - \left(B_f^{(1)}(t)\right)^2} \quad (23)$$

in which $B_f^{(1)}(t)$ is the mean Doppler shift presented in (21).

With the same token, the instantaneous Doppler spread can also be derived from the spectrogram $S_{xx}(f, t)$ in (19). It follows [19]

$$B_{xx}^{(2)}(t) = \sqrt{\frac{\int_{-\infty}^{+\infty} f^2 S_{xx}(f, t) df}{\int_{-\infty}^{+\infty} S_{xx}(f, t) df} - \left(B_{xx}^{(1)}(t)\right)^2} \quad (24)$$

where $B_{xx}^{(1)}(t)$ is the mean Doppler shift in (22) obtained from the spectrogram approach.

The simulation results (see Sec. VI) will show that $B_f^{(2)}(t)$ and $B_{xx}^{(2)}(t)$ are in close agreement.

VI. SIMULATION RESULTS

A. Parameter Settings and Procedures

It is assumed that the propagation area consists of a cluster of $N_M = 5$ moving scatterers, accounting for the head, hands, and the legs of the home user, as well as the number of $N_F = 5$ fixed scatterers¹². A person with an actual height H of 178 cm is considered. For such a height, experimental results [31] show that the parameter α_h is about 2.7 cm and the step length is about 73 cm, allowing for the gait

¹²The body parts are of course more than those considered in this paper. The neck, chest, abdomen, elbows, and the feet are examples of other parts that influence the propagation mechanism. To which extent and which form (scattering/reflection/diffraction) is a question that can hardly be answered. In this paper, our aim is to develop a realistic model that can fairly explain the propagation mechanism in the presence of a human body represented as a cluster of moving objects. As the paper concludes later, the proposed channel model is able to deliver verifiable characteristics with the consideration of only five moving scatterers (representing the five body parts). We remark that in the context of radio channel modelling, the higher number of scatterers adds to the complexity of the model due to parametrization tasks and theoretical analysis artefact (e.g., cross-terms of spectrogram analysis). In this context, studying the impact of number of scatterers and/or their sizes on the modelling performance is a topic worth studying, but is not the objective of this paper.

frequency w_G of nearly π . It is assumed that the home user starts walking from the origin $(x_s, y_s) = (0 \text{ m}, 0 \text{ m})$ of the Cartesian coordinates¹³ to reach the preplanned destination point $(x_d, y_d) = (3 \text{ m}, 4 \text{ m})$ via a single realization of the 3D random trajectory \mathcal{T} . The trajectory of a normal walk consists of 1200 points indexed by $l = 1$ (starting point) until $l = L = 1200$ (destination point), allowing for a comparable resolution with respect to our measurement results. The initial phase θ_0 of the gait cycle is assumed to be zero. The maximum distance σ_{\max} from the shortest trajectory (straight path) is set to 1 m.

The user starts accelerating from a zero speed to a constant walking speed within l_C steps. The vertical (horizontal) speed of the person within the walking phase is set to 0.1 m/s (1 m/s), i.e., $s_{n_M, l}^h = 1 \text{ m/s}$ ($s_{n_M, l}^v = 0.1 \text{ m/s}$) for all $n_M = 1, 2, \dots, 5$ and $l = l_C, \dots, l_{FP} - 1$. These values are in line with those obtained from video signal processing in [33] and close to those reported in [45]. If a fall does not happen (l_{FP} does not exist), the person keeps walking at the same speed. Otherwise, the whole body starts accelerating to a final speed of $s_{n_M, l_{FP} + L_F}^{(\cdot)} = 2.5 \text{ m/s}$ within L_F steps. When the falling phase is completed, the user is assumed to be motionless along all directions.

The operating frequency of $f_0 = 5.9 \text{ GHz}$ is considered in our simulations. The same frequency was used before to collect empirical results from an indoor radio measurement campaign [18]. As shown in Fig. 2, Tx and Rx are assumed to be placed on the floor and the ceiling of the room, respectively. The free-space path loss exponent is set to $\gamma = 2$, which suits best to our lossless single-bounce scattering scenario, while the constant C is set to 1.

Given the settings above, the simulation results have been produced by taking the following steps: 1) The number of 5 trajectories have been generated according to a single realization of (3), but placed at different starting points (of the motion) (x_s, y_s, z_h) . For instance, we have considered a sample scatterer at $(0, 0, 1.78) \text{ m}$ to account for the head, while the right leg is represented by a sample scatterer with initial coordinates of $(0.2, 0.2, 0.4) \text{ m}$. The forward fall mechanism (see Sec. II-B) has been applied if needed; 2) When the trajectories are generated, the 3D coordinate of each point scatterer is fully known all along the path. Given two consecutive points, the elevation (azimuth) angle of motion is computed using simple tangent relationships. The positions of the Tx and Rx are also known. Then, the elevation (azimuth) angle of arrival (departure) at (from) each point is computed. From the calculated quantities, 3) the Doppler shifts $f_{n_M}(l)$ have been computed (see (9)); 4) The spectral characteristics, including the local Doppler PSD, spectrogram, instantaneous mean Doppler shift, and the instantaneous Doppler spread have been computed according to their equations derived in Sec.V; 5) The results have been demonstrated and interpreted.

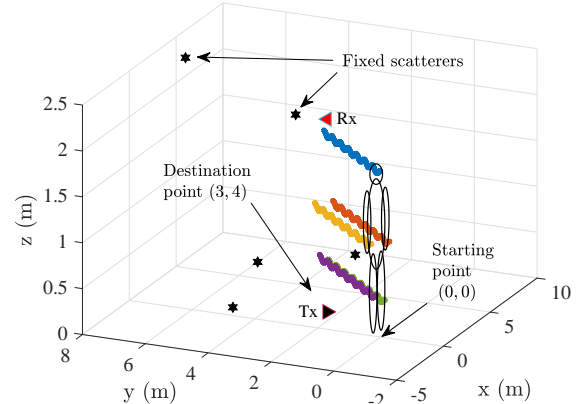


Fig. 2. An in-home propagation area, illustrating the trajectory of the home user in a non-falling scenario.

B. Results

Figs. 2 and 3 illustrate the trajectories of the cluster of 5 moving scatterers (representing the home user) for the non-falling and falling scenarios, respectively. The user starts walking from the origin and aims at reaching the shown destination point. In the non-falling scenario, the user arrives successfully at the destination point after about $t = 10 \text{ s}$, whereas in the falling scenario, the user fails to do so because of a random fall incident happened at $t = 6.3 \text{ s}$ (or equivalently $l_{FP} = 780$). The falling phase is completed within $L_F = 100$ steps, allowing for a forward fall of about 1 m length in the x - y plane and along the planned trajectory. For given s^v and s^h vectors (of length 100) associated with the increasing vertical and horizontal speed profiles of the user within the falling phase (see Secs. II-C and VI-A), the acceleration vectors a^v and a^h can be obtained. It follows that the falling phase is completed within 0.8 s, indicating a normal fall. With reference to both figures, the proposed trajectory model can capture sinusoidal oscillations of the body seen in actual human walks. Ignoring these small-scale vertical oscillations, it can be seen that the large-scale distance between the cluster of moving scatterers (mobile user) and the transceiver first decreases and then increases. This increase is followed by the continuation of the normal walk towards the destination point (see Fig.2) or by the occurrence of the fall (see Fig.3).

The signal envelope $|\mu(t)|$ (see (5)) corresponding to both falling and non-falling scenarios is shown in Fig. 4. Both curves show the fading behavior of the indoor channel within the observation time. Within the falling phase, i.e., $6.3 \leq t \leq 7.1 \text{ s}$, the curves associated with the falling scenario shows more fluctuations, but still cannot be readily distinguished from that of the non-falling scenario. This indicates the difficulty of recognizing rapid variations of the channel in the time domain, thus motivating us to investigate the spectral properties of the channel. After completion of the fall, the complex channel gain $\mu(t)$ in (5) becomes time-invariant, resulting in a constant signal envelope for $t \geq 6 \text{ s}$, wherefrom the two curves become discernible. It is, however, noteworthy that in real-world indoor channels, where moving scatterers

¹³The x - y plane (home floor) is sufficient for addressing the starting and the terminating point of the walking user at home.

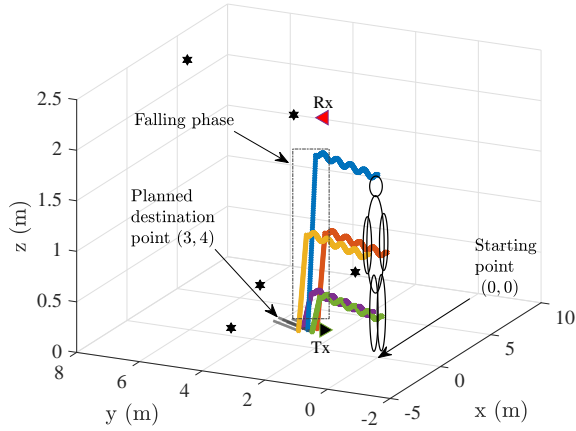


Fig. 3. An in-home propagation area, illustrating the trajectory of the home user in a falling scenario.

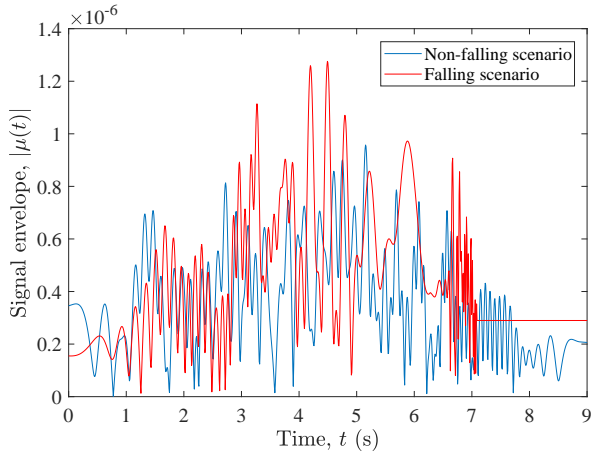


Fig. 4. The signal envelope $|\mu(t)|$ (see (5)) associated with the falling and the non-falling scenarios.

are inherent elements of the propagation area, such a time-invariant signal envelop can hardly be measured. Developing more advanced channel models capturing permanent moving scatterers is therefore a topic for our future studies.

Fig. 5 demonstrates the local Doppler PSD $S_f(f, t)$ (see (16)) of the channel for the non-falling scenario. At each time instant (position index l), there exist 5 Dirac delta functions associated with the Doppler shifts of the plane waves arriving from the five moving scatterers. As time passes and the path evolves (see 2), the position of these delta functions and their magnitude experience some small-scale fluctuations due to the vertical oscillations of the scatterers, and some large-scale changes caused by the main mobility pattern of those scatterers in the horizontal plane. For the first three seconds, the Doppler shifts $f_{n_M}(t)$ increase from zero (initial stop) to about 15 Hz, confirming the initial acceleration of the user for a normal walk. As the user approaches the vicinity of the RX/TX, the Doppler shifts $f_{n_M}(t)$ decrease and the magnitudes $c_{n_M}^2(t)$ increase. The decrease in the Doppler shifts is due to the fact that the AOA (AODs) at(from) the scatterers approach the right angle (90°), while the increase

in the magnitudes can be attributed to the path loss effect captured by $c_{n_M}(t) = CD_{n_M}^{-\gamma}(t)$ (see Sec. IV). This trend holds until almost the middle of the path, wherefrom the user starts distancing from the transceiver, explaining the reduction of the received power and the enlargement of the Doppler frequency shifts towards negative values. For $t > 7$, the Doppler components vanish, as the person start decelerating to a zero speed. The small-scale fluctuations of the PSD in time (position) originate from the sinusoidal movements of the scatterers along the z -axis. Other settings of Tx/Rx can magnify such variations.

Fig. 6 exhibits the spectrogram $S_{xx}(f, t)$ (see (19)) of the process $\mu(t)$ associated with the non-falling scenario using a Gaussian window of size $\sigma_\omega = 50$ ms. The figure shows the time-frequency distribution of $\mu(t)$ as the person walks in the room. The illustrated spectrogram $S_{xx}(f, t)$ provides an estimation of the local Doppler PSD $S_f(f, t)$ of the process $\mu(t)$ shown in Fig. 5. In line with our previous observations, $S_{xx}(f, t)$ shows an S-shape within ± 15 Hz, demonstrating oscillatory frequency components that change in time. These frequency components are positive within almost the first 4 seconds, as the user approaches the Tx/Rx, then become negative as the user leaves the transceiver. The higher values of $S_{xx}(f, t)$ around $t = 4$ s and/or $f = 0$ Hz are due to the shorter travelling distances of radio waves at the vicinity of Tx/Rx. The oscillatory behavior of the frequency components is caused by the height variations of the user within a normal walk process. The time-invariant zero frequency component is due to the presence of fixed scatterers in the propagation environment, while the time-invariant spread around $f = 0$ Hz is an artifact caused by the spectrogram analysis. Note that the spectrogram analysis suffers from physically unexplainable artifacts in form of interfering cross-terms [43]. The zero frequency (and the corresponding spread) cannot be observed in Fig. 5, as $S_f(f, t)$ in (16) models only non-zero Doppler frequencies caused by moving scatterers.

Fig. 7 shows the Doppler PSD $S_f(f, t)$ of the falling scenario. Before occurring the fall at $t = 6.3$ s, the curve behaves very similar to that of the non-falling scenario. The minor differences are due to the randomness of the proposed trajectory model, which has resulted in 2 different, yet statistically similar, trajectories. When the fall incident occurs, the PSD tends sharply towards negative Doppler shifts. This is because of the rapid departure (falling down) of the cluster of moving scatterers from the receiver (mounted on the ceiling) towards the floor. The considerable growth of the vertical/horizontal speed within the falling phase results in the remarkable rise of the Doppler shifts from about -10 Hz to -50 Hz within just 0.8 s. A second large variation of the PSD is observed at $t = 7.1$ s, when the falling phase is completed and the user becomes motionless. This results in a zero Doppler shift for $t > 7.1$ s. It is also worth-mentioning that when the fall occurs, the trajectory of the user along the z -axis is determined by the height reduction mechanism in (4), thus no more oscillatory variations of the PSD can be seen.

Fig. 8 represents the results of the spectrogram $S_{xx}(f, t)$ (see (19)) analysis associated with the falling scenario using a Gaussian window with the spread parameter $\sigma_\omega = 0.03$ s.

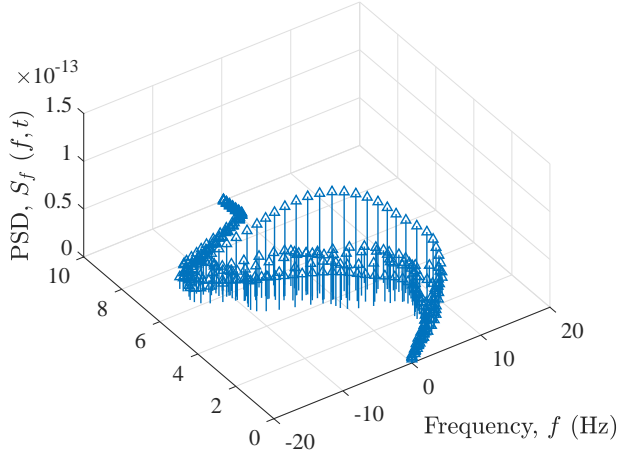


Fig. 5. The PSD $S_f(f, t)$ (see (16)) of the Doppler frequencies $f_{n_M}(t)$ for the non-falling scenario.

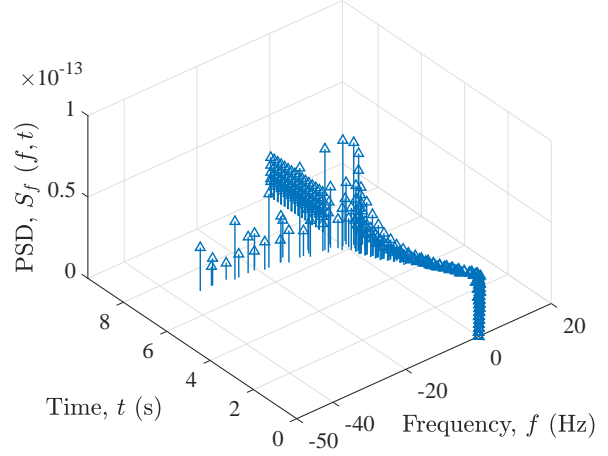


Fig. 7. The PSD $S_f(f, t)$ (see (16)) of the Doppler frequencies $f_{n_M}(t)$ for the falling scenario.

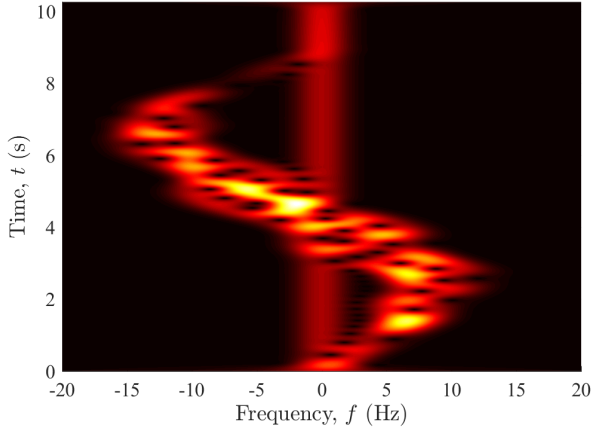


Fig. 6. The spectrogram $S_{xx}(f, t)$ (see (19)) of the complex channel gain process $\mu(t)$ for the non-falling scenario.

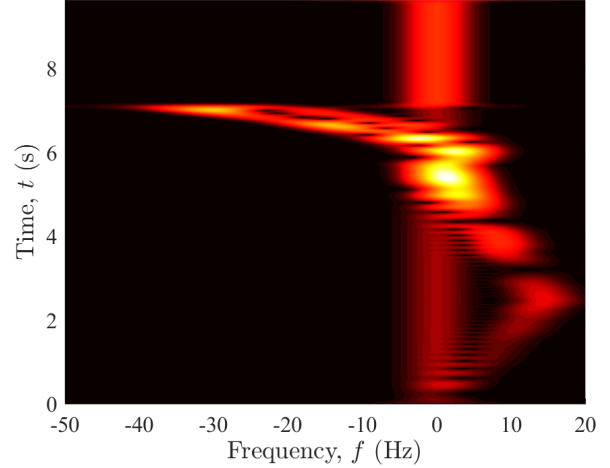


Fig. 8. The spectrogram $S_{xx}(f, t)$ (see (19)) of the complex channel gain process $\mu(t)$ for the falling scenario.

Similar to the observations in Fig. 7, $S_{xx}(f, t)$ contains frequency components that changes in time, confirming the non-stationarity of the proposed channel model. These frequency components are oscillatory within the first 6.3 seconds, as the user is walking normally towards the Tx/Rx. Upon the occurrence of the fall, the Doppler frequency components rise significantly to -50 Hz within just 0.8 s. When the fall is completed, those negative frequency components turn suddenly into near-zero frequency components, as the user become static, adding to the impact of static objects in the room. For $t \geq 7.1$ s, the time-invariant frequency spread around $f = 0$ Hz is generated by the interfering cross-terms caused by spectrogram analysis. Comparing Figs. 6 and 8, one can observe the major difference between the order of the Doppler shifts appearing as a result of a fall incident and/or a normal walk. This major difference can assist system designers in the development of robust detection algorithms based on the time-frequency behavior of the channel.

Fig. 9 demonstrates the instantaneous Doppler spread $B_f^{(2)}(t)$ and $B_{xx}^{(2)}(t)$ obtained from (23) and (24), respectively.

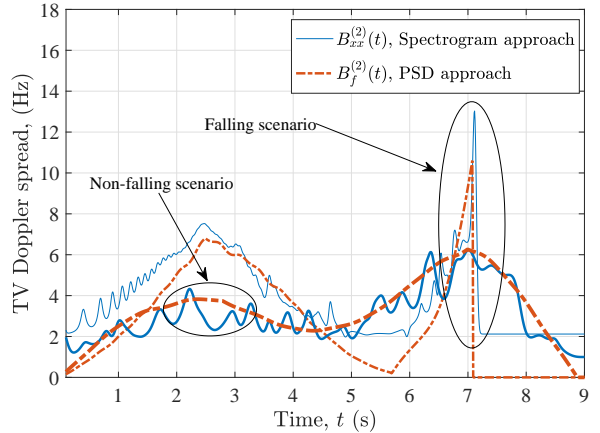


Fig. 9. The instantaneous Doppler spread $B_f^{(2)}(t)$ and $B_{xx}^{(2)}(t)$ obtained from two different approaches (see (23) and (24)) and associated with the falling and the non-falling scenarios.

Before $t = 6.3$ s, both pair of curves show similar fluctuating behaviour. The difference between the curves of each pair is due to the cross-term interference (as discussed before), while the difference between the two pairs is caused by the employed random trajectories generated by (3). The general reduction of the Doppler spread at around $t = 4$ s, when the AOM is almost perpendicular to the AOA, is because of the convergence of all TV Doppler shifts to zero. When the fall occurs, the Doppler spread increases significantly. This is due to the major and diverse contribution of the AOMs (of the body parts) to the Doppler shift. After the falling phase, $B_f^{(2)}(t)$ vanishes because all Doppler shifts converge to zero. However, $B_{xx}^{(2)}(t)$ reduces to a non-zero value, which remains constant over time. This non-zero Doppler spread is attributed to the frequency components of cross-terms interfering the spectrogram analysis. A similar observation can be made in Fig. 8, where some time-invariant frequency components remain even after the completion of the fall at $t = 7.1$ s. The sharp peak of the Doppler spread within the falling phase is about 3 times larger than the average Doppler spread within the walking phase, also differs significantly from the near-zero Doppler spread after the completion of the fall. Accordingly, the instantaneous Doppler spread can be considered as an indication of a fall incident, thus can be used for the design of fall detection algorithms.

C. Verification with Empirical Results

In this section, the mean Doppler shift obtained from the spectrogram approach and the PSD approach are validated by the empirical results collected from a radio measurement campaign performed at 5.9 GHz [18]. In the experiment, the performer is asked to walk at an elderly speed, while approaching the Tx/Rx at the first couple of seconds and then leaving the Tx/Rx along the predefined path. To match the simulation model against the empirical data, we have chosen similar values for the length of the trajectory, its direction, position of the Tx/Rx, position of the fall, and the speed of the user as briefed in VI-A. The empirical mean Doppler shift has been computed by applying the principle of the spectrogram analysis (see V) to the measured complex channel gain.

Fig. 10 displays the instantaneous mean Doppler shift $B_{xx}^{(1)}(t)$ obtained from the spectrogram approach, $B_f^{(1)}(t)$ obtained from the PSD approach, and the empirical results collected from the indoor measurement campaign. The curves have been obtained after filtering time-invariant near-zero frequencies (see, e.g., those in Fig. 6) due to the fixed objects. The three curves are in a good agreement with each other and with our previous observations (the S-shape). The difference between $B_{xx}^{(1)}(t)$ and $B_f^{(1)}(t)$ is expectable, as it is caused by the fundamental difference between the two employed approaches. The spectrogram approach comes with cross-terms (computational interference) that affect the instantaneous mean Doppler shift $B_{xx}^{(1)}(t)$, whereas $B_f^{(1)}(t)$ is obtained from the interference-free Doppler PSD (see (16)). In the normal walking phase, both curves show a fluctuating increase as the person moves towards the transceiver. At the first glance, this is in contract with our previous observations

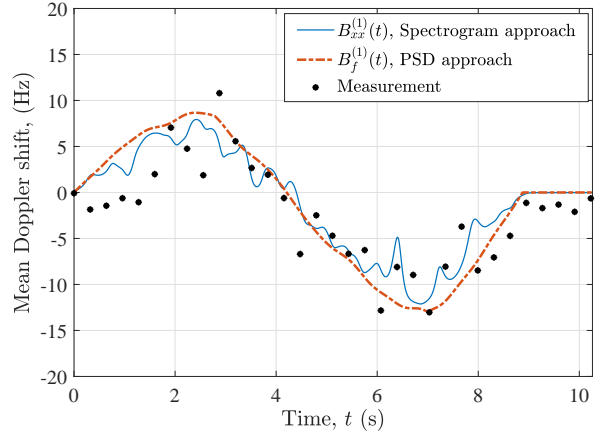


Fig. 10. The instantaneous mean Doppler shift $B_f^{(1)}(t)$ and $B_{xx}^{(1)}(t)$ obtained from two different approaches (see (21) and (22)) in comparison with the measured mean Doppler shift of the non-falling scenario.

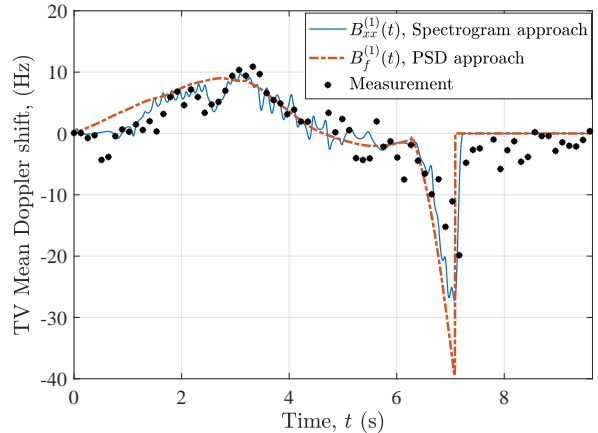


Fig. 11. The instantaneous mean Doppler shift $B_f^{(1)}(t)$ and $B_{xx}^{(1)}(t)$ obtained from two different approaches (see (21) and (22)) in comparison with the measured mean Doppler shift of the falling scenario.

and heuristic expectations, where the Doppler shifts should decrease when moving towards the transceiver. However, this can be explained by the increase in the path gains (shorter wave travelling distance) as the weighting factors of the mean Doppler shift. At almost $t = 4$ s, the perpendicularity of the radio waves to the direction of motion dominates over the increasing path gains and reduces the mean Doppler shift to the zero level. Hereafter, the waves arrive (depart) at (from) the back of the walking person, which results in negative mean Doppler shifts. This trend holds as long as the person walks along the path. When the person decelerate to come to a full stop at the end of the trajectory, the Doppler shifts vanish, allowing for a zero mean Doppler shift at around $t = 10$ s. The behavior of the mean Doppler shift explained above complies with the mobility pattern of the user, who was asked to first approaches the Tx/Rx and then to leave the Tx/Rx in the corresponding experiment (see Sec. II-B and Fig. 2 in [18]).

The corresponding three curves associated with the falling scenario are shown in Fig. 11. A very good match between the simulation results and empirical results can be observed. When

the fall occurs at $t = 6.3$ s, the mean Doppler shift reduces to -20 Hz. After the completion of the fall, i.e., $t \geq 7.1$ s, the theoretical mean returns to absolute zero, while the empirical mean stays on near-zero values. This can be caused by very slowly moving objects in the experiment environment. Note that the obtained instantaneous Doppler frequency components can reach up to -50 Hz (see Fig.8), but the corresponding weighted mean is twice of that of a normal walking scenario. Nonetheless, the difference between the TV mean Doppler shift in Figs. 10 and 11 is completely visible. Accordingly, one may consider the instantaneous mean Doppler shift as a robust fall detection algorithm design metric.

VII. DISCUSSION

It is noteworthy that some daily-life activities can imprint the time-frequency distribution of the channel with similar signatures to those of fall incidents. Lying in bed, sitting on chair or ground, jumping over a couple of stairs, and chaotic movements of pets are examples of activities that either have similar trajectory and/or temporal features to that of a falling incident¹⁴. To reduce the number of potential false alarms caused by such activities, the utilization of machine learning models has been proposed in the literature (see the systems based on the learning method in [26]). The application of deep learning techniques has also been proposed in [46]. Those models can be improved by employing the data obtained from the spectrogram analysis as an additional training dataset (feature).

Our recent experimental studies (not presented here) show that other channel characteristics, such as the level-crossing rate and the PDP are also influenced by the activities of the home user. For instance, the channel envelope shows a higher number of fluctuations within the falling phase and a relatively stable level after the completion of the falling phase. Such variations have already been utilized for the development of RSSI-based activity recognition algorithms (see Sec. I). Nonetheless, our results confirm that fingerprints of the human activity are more visible and explainable in the time-frequency distribution of the channel compared to those in the time domain. The frequency-domain characteristics of the channel have also been used for the development of device-free tracking systems. As an example, the WiTrack system utilizes a frequency modulated carrier wave (FMCW) radar to track 3D motions of a user [47]. This technology was then used to develop a preventative product called Emerald, which allows for both detecting falls and monitoring its precursors [48].

We remark that the experimental results presented in this paper were obtained using an advanced radio channel sounder that allows us to perform very detailed time-frequency analysis. Such measurement instruments are often very costly, thus they are not recommended for prototyping purposes. For developing a system prototype, commercial WiFi network

interference controllers and/or software defined radio units are recommended.

It is also noteworthy that employing multiple antennas can improve the performance of recognitions. Indeed, the resultant spatial diversity allows for receiving multiple fingerprints of the home occupant on the channel characteristics. These copies can help us to develop more reliable detection algorithms that work based on combined metrics rather than a single one. An example of such a system is PhaseBeat, where CSI phase difference data was used to monitor breathing and heartbeat with commodity WiFi devices [49]. More recently, the multiple antenna approach has also been used in the development of a non-contact respiratory rhythm-detection system using S-band sensing techniques [50].

VIII. CONCLUSION

In this paper, we have proposed an indoor non-stationary channel model that can be used for the development of emerging non-wearable radio fall detection systems. The model consists of a stochastic 3D trajectory model to capture the mobility pattern of the user, a cluster of moving scatterers to account for the body parts of the home user, some fixed scatterers to consider static objects in the room, and a transmitter/receiver to rule the radio communications. The proposed trajectory model has been featured with a height reduction mechanism along the planned path, permitting for the simulation of a forward fall incident at a random point. The complex channel gain has been modelled by a stochastic process, capturing the TV Doppler effect caused by the mobility pattern of the home user. It has been shown that the falling phase can hardly be studied just by focusing on the signal envelope in the time domain. Accordingly, the time-frequency behavior of the non-stationary radio channel has been studied through two different approaches, namely the local PSD approach and the spectrogram approach. It has been shown that both approaches result in similar time-frequency observations. Other spectral properties of the channel, including the instantaneous mean Doppler shift and the instantaneous Doppler spread have been derived and studied. The simulation results have been verified by the empirical ones collected from a radio measurement campaign performed at 5.9 GHz. Simulation results have been demonstrated for both a falling scenario and a non-falling scenario, showing the responsiveness of the spectral properties to the variations of the channel. It has been shown that both the Doppler PSD and the spectrogram of the complex channel gain are fingerprinted by the mobility of the home user, while the instantaneous mean Doppler shift and the instantaneous Doppler spread render visible signs of the fall incident. It is concluded that the spectrogram analysis is a very sound and practical approach not only for tracking fingerprints of the fall incident on the time-frequency distribution of the channel, but also for studying the mobility characteristics of the home user.

Future studies on the development of fall detection algorithms based on spectral channel properties are needed. The robustness of those algorithms with respect to false alarms needs to be examined in real-world settings. To increase the reliability of the overall system, detection algorithms should

¹⁴As an example, a sitting action is normally performed at a lower speed than a falling incident, especially if the performer is an elderly. Given the fact that the speed of a scatterer directly affects the Doppler shift (see (7)), this activity results in Doppler shifts smaller than those of the falling incident. Such differences can be utilized to improve the training phase of a machine learning model.

be designed based on multiple spectral channel characteristics, rather than one and/or just temporal ones. Conducting detailed radio measurement campaigns at other frequency bands is needed for the further development of this research line. Other characteristics of the channel, such as the PDP and the level-crossing rate, are expected to contain useful information on the variations of the propagation environment. The proposed channel model can also be studied under other configurations of the trajectory, falling styles, and other speed profiles of the home user.

ACKNOWLEDGMENT

This work was supported by the WiCare Project funded by the Research Council of Norway under grant number 261895/F20. The authors would also like to acknowledge the valuable comments from the anonymous reviewers of this paper.

REFERENCES

- [1] Daniel Goodkind Wan He and Paul Kowal, "An aging world: 2015," *Int. Population Reports*, March 2016.
- [2] Department of Ageing and Life Course, "WHO global report on falls prevention in older age," 2007.
- [3] B. Erol and M. G. Amin, "Fall motion detection using combined range and Doppler features," in *2016 24th European Signal Processing Conference (EUSIPCO)*, Aug 2016, pp. 2075–2080.
- [4] Zhong Zhang, Christopher Conly, and Vassilis Athitsos, "A survey on vision-based fall detection," in *Proceedings of the 8th ACM Int. Conf. on Pervasive Technologies Related to Assistive Environments*, New York, NY, USA, 2015, PETRA '15, pp. 46:1–46:7, ACM.
- [5] C. Rougier, J. Meunier, A. St-Arnaud, and J. Rousseau, "Robust video surveillance for fall detection based on human shape deformation," *IEEE Transactions on Circuits and Systems for Video Technology*, vol. 21, no. 5, pp. 611–622, May 2011.
- [6] H. Rimminen, J. Lindström, M. Linnavuori, and R. Sepponen, "Detection of falls among the elderly by a floor sensor using the electric near field," *IEEE Trans. Inform. Tech. in Biomedicine*, vol. 14, no. 6, pp. 1475–1476, Nov 2010.
- [7] Muhammad Mubashir, Ling Shao, and Luke Seed, "A survey on fall detection: Principles and approaches," *Neurocomputing*, vol. 100, pp. 144 – 152, 2013, Special issue: Behaviours in video.
- [8] L. Zhu, P. Zhou, A. Pan, J. Guo, W. Sun, L. Wang, X. Chen, and Z. Liu, "A survey of fall detection algorithm for elderly health monitoring," in *2015 IEEE Fifth International Conference on Big Data and Cloud Computing*, Aug 2015, pp. 270–274.
- [9] O. D. Lara and M. A. Labrador, "A survey on human activity recognition using wearable sensors," *IEEE Communications Surveys Tutorials*, vol. 15, no. 3, pp. 1192–1209, Third 2013.
- [10] Yueng Santiago Delahoz and Miguel Angel Labrador, "Survey on fall detection and fall prevention using wearable and external sensors," *Sensors*, vol. 14, no. 10, pp. 19806–19842, 2014.
- [11] Q. Wu, Y. D. Zhang, W. Tao, and M. G. Amin, "Radar-based fall detection based on Doppler time-frequency signatures for assisted living," *IET Radar, Sonar Navigation*, vol. 9, no. 2, pp. 164–172, 2015.
- [12] B. Y. Su, K. C. Ho, M. J. Rantz, and M. Skubic, "Doppler radar fall activity detection using the wavelet transform," *IEEE Transactions on Biomedical Engineering*, vol. 62, no. 3, pp. 865–875, March 2015.
- [13] B. Erol, M. G. Amin, and B. Boashash, "Range-Doppler radar sensor fusion for fall detection," in *2017 IEEE Radar Conference (RadarConf)*, May 2017, pp. 0819–0824.
- [14] A. Shrestha, J. Le Kernec, F. Fioranelli, E. Cippitelli, E. Gambi, and S. Spinsante, "Feature diversity for fall detection and human indoor activities classification using radar systems," in *International Conference on Radar Systems (Radar 2017)*, Oct 2017, pp. 1–6.
- [15] K. Shiba, T. Kaburagi, and Y. Kurihara, "Fall detection utilizing frequency distribution trajectory by microwave Doppler sensor," *IEEE Sensors Journal*, vol. 17, no. 22, pp. 7561–7568, Nov 2017.
- [16] L. Yao, Q. Z. Sheng, X. Li, T. Gu, M. Tan, X. Wang, and W. Zou, "Compressive representation for device-free activity recognition with passive RFID signal strength," *IEEE Transactions on Mobile Computing*, no. 99, pp. 1–1, 2017.
- [17] G. Mokhtari, Q. Zhang, and A. Fazlollahi, "Non-wearable UWB sensor to detect falls in smart home environment," in *2017 IEEE International Conference on Pervasive Computing and Communications Workshops (PerCom Workshops)*, March 2017, pp. 274–278.
- [18] F. Firoozi, A. Borhani, and M. Pätzold, "Experimental characterization of mobile fading channels aiming the design of non-wearable fall detection radio systems at 5.9 GHz," in *2016 IEEE International Conference on Communication Systems (ICCS)*, Dec 2016, pp. 1–6.
- [19] A. Abdelgawwad and M. Pätzold, "On the influence of walking people on the Doppler spectral characteristics of indoor channels," in *Personal Indoor and Mobile Radio Communications (PIMRC)*, Oct 2017, Montreal, Canada.
- [20] Y. Wang, K. Wu, and L. M. Ni, "WiFall: Device-free fall detection by wireless networks," *IEEE Transactions on Mobile Computing*, vol. 16, no. 2, pp. 581–594, Feb 2017.
- [21] D. Halperin, W. Hu, A. Sheth, and D. Wetherall, "Tool release: Gathering 802.11n traces with channel state information," *ACM SIGCOMM Computer Communication Review*, vol. 41, no. 1, pp. 53–53, Jan 2011.
- [22] R. Ramezani, Y. Xiao, and A. Naïm, "Sensing-Fi: Wi-Fi CSI and accelerometer fusion system for fall detection," in *2018 IEEE EMBS International Conference on Biomedical Health Informatics (BHI)*, March 2018, pp. 402–405.
- [23] H. Wang, D. Zhang, Y. Wang, J. Ma, Y. Wang, and S. Li, "RT-Fall: A real-time and contactless fall detection system with commodity WiFi devices," *IEEE Transactions on Mobile Computing*, vol. 16, no. 2, pp. 511–526, Feb 2017.
- [24] Sameera Palipana, David Rojas, Piyush Agrawal, and Dirk Pesch, "FallDeFi: Ubiquitous fall detection using commodity Wi-Fi devices," *Proc. ACM Interact. Mob. Wearable Ubiquitous Technol.*, vol. 1, no. 4, pp. 155:1–155:25, Jan. 2018.
- [25] Yaxiong Xie, Zhenjiang Li, and Mo Li, "Precise power delay profiling with commodity WiFi," in *Proceedings of the 21st Annual International Conference on Mobile Computing and Networking*, New York, NY, USA, 2015, MobiCom '15, pp. 53–64, ACM.
- [26] H. Jiang, C. Cai, X. Ma, Y. Yang, and J. Liu, "Smart Home Based on WiFi Sensing: A Survey," *IEEE Access*, vol. 6, pp. 13317–13325, 2018.
- [27] B. Mager, N. Patwari, and M. Bocca, "Fall detection using rf sensor networks," in *2013 IEEE 24th Annual International Symposium on Personal, Indoor, and Mobile Radio Communications (PIMRC)*, Sept 2013, pp. 3472–3476.
- [28] S. Kianoush, S. Savazzi, F. Vicentini, V. Rampa, and M. Giussani, "Leveraging RF signals for human sensing: Fall detection and localization in human-machine shared workspaces," in *2015 IEEE 13th International Conference on Industrial Informatics (INDIN)*, July 2015, pp. 1456–1462.
- [29] S. Kianoush, S. Savazzi, F. Vicentini, V. Rampa, and M. Giussani, "Device-free RF human body fall detection and localization in industrial workplaces," *IEEE Internet of Things Journal*, vol. 4, no. 2, pp. 351–362, April 2017.
- [30] A. Borhani and M. Pätzold, "A highly flexible trajectory model based on the primitives of Brownian fields—Part I: Fundamental principles and implementation aspects," *IEEE Trans. Wireless Commun.*, vol. 14, no. 2, pp. 770–780, Feb. 2015.
- [31] J. Rose and J. G. Gamble, *Human Walking*, Williams & Wilkins, 1994.
- [32] A. Borhani and M. Pätzold, "A highly flexible trajectory model based on the primitives of Brownian fields—Part II: Analysis of the statistical properties," *IEEE Trans. Wireless Commun.*, vol. 15, no. 1, pp. 247–257, Jan. 2016.
- [33] H. Foroughiand, M. Alishah, H. Pourreza, and M. Shahinfar, *Distinguishing Fall Activities using Human Shape Characteristics*, pp. 523–528, Springer Netherlands, Dordrecht, 2010.
- [34] G. Stüber, *Principles of Mobile Communications*, Springer, 3rd edition, 2011.
- [35] B. Boashash, *Time-Frequency Signal Analysis and Processing*, Elsevier Science, 1st edition, 2003.
- [36] T. K. Sarkar, Z. Ji, K. Kim, A. Medouri, and M. Salazar-Palma, "A survey of various propagation models for mobile communication," *Antennas and Propagation Magazine, IEEE*, vol. 45, no. 3, pp. 51–82, June 2003.
- [37] C. Phillips, D. Sicker, and D. Grunwald, "A survey of wireless path loss prediction and coverage mapping methods," *Communications Surveys Tutorials, IEEE*, vol. 15, no. 1, pp. 255–270, 2013.

- [38] M. Pätzold, *Mobile Fading Channels*, Chichester: John Wiley & Sons, 2nd edition, 2011.
- [39] V. H. Pham, M. H. Taieb, J. Y. Chouinard, S. Roy, and H. T. Huynh, "On the double Doppler effect generated by scatterer motion," *REV Journal on Electronics and Communications*, vol. 1, no. 1, pp. 30–37, Mar. 2011.
- [40] R. E. Moritz, *A Text Book on Spherical Trigonometry*, Jon Wiley & Sons, 1913.
- [41] A. Borhani, G. L. Stüber, and M. Pätzold, "A random trajectory approach for the development of nonstationary channel models capturing different scales of fading," *IEEE Transactions on Vehicular Technology*, vol. 66, no. 1, pp. 2–14, Jan 2017.
- [42] M. Pätzold and C. A. Gutiérrez, "Enhancing the resolution of the spectrogram of non-stationary mobile radio channels by using massive MIMO techniques," in *Proc. IEEE 86th Vehicular Technology Conference, VTC2017-Fall*. Toronto, Canada.
- [43] M. Pätzold and C. A. Gutiérrez, "Spectrogram analysis of multipath fading channels under variations of the mobile speed," in *2016 IEEE 84th Vehicular Technology Conference (VTC-Fall)*, Sept 2016, pp. 1–6.
- [44] M. Pätzold, C. A. Gutiérrez, and N. Youssef, "On the consistency of non-stationary multipath fading channels with respect to the average doppler shift and the doppler spread," in *2017 IEEE Wireless Communications and Networking Conference (WCNC)*, March 2017, pp. 1–6.
- [45] P. Y. Loh S. Muraki I. N. Afiah, H. Nakashima, "An exploratory investigation of changes in gait parameters with age in elderly japanese women," *SpringerPlus*, vol. 5, no. 1069, pp. 1–14, Jul 2016.
- [46] S. Yousefi, H. Narui, S. Dayal, S. Ermon, and S. Valaee, "A survey on behavior recognition using WiFi channel state information," *IEEE Communications Magazine*, vol. 55, no. 10, pp. 98–104, OCTOBER 2017.
- [47] Fadel Adib, Zachary Kabelac, Dina Katabi, and Robert C. Miller, "3d tracking via body radio reflections," in *Proceedings of the 11th USENIX Conference on Networked Systems Design and Implementation*, Berkeley, CA, USA, 2014, NSDI'14, pp. 317–329, USENIX Association.
- [48] D. Katabi et al., "Emerald," in <http://www.emeraldforhome.com/>.
- [49] X. Wang, C. Yang, and S. Mao, "PhaseBeat: Exploiting CSI phase data for vital sign monitoring with commodity WiFi devices," in *2017 IEEE 37th International Conference on Distributed Computing Systems (ICDCS)*, June 2017, pp. 1230–1239.
- [50] D. Fan, A. Ren, N. Zhao, X. Yang, Z. Zhang, S. A. Shah, F. Hu, and Q. H. Abbasi, "Breathing rhythm analysis in body centric networks," *IEEE Access*, vol. 6, pp. 32507–32513, 2018.



Matthias Pätzold (M'94-SM'98) received the Dipl.-Ing. and Dr.-Ing. degrees in electrical engineering from Ruhr-University Bochum, Bochum, Germany, in 1985 and 1989, respectively, and the habil. degree in communications engineering from the Technical University of Hamburg-Harburg, Germany, in 1998. From 1990 to 1992, he was with ANT Nachrichtentechnik GmbH, Backnang, Germany, where he was engaged in digital satellite communications. From 1992 to 2001, he was with the department of digital networks at the Technical University Hamburg-Harburg. Since 2001, he has been a full professor of mobile communications with the University of Agder, Norway. He authored several books and numerous technical papers. His publications received ten best paper awards. He has been actively participating in numerous conferences serving as TPC chair and TPC member.



Alireza Borhani (S'12-M'14) received the Ph.D. degree and the M.E. degree both in Telecommunications Engineering from University of Agder in Norway and University of Shahed in Iran, respectively. He also received the B.E. degree in Electrical Engineering-Biomedical Systems from the Science and Research branch of Azad University in Tehran. Since 2011, he is with the mobile communications group at the University of Agder, Norway. He has been actively participating in numerous conferences serving as TPC chair and TPC member. His research

interests include signal processing, data analytics, healthcare IoT, radio communications, and information theory.